12th International Symposium on Turbulence and Shear Flow Phenomena (TSFP12)
Osaka, Japan, July 19–22, 2022

HYDRODYNAMICS OF A COW-NOSED RAY (RHINOPTERA JAVANICA) IN FORWARD SWIMMING AT A HIGH REYNOLDS NUMBER

Dong Zhang
Department of Engineering Mechanics
Tsinghua University
Beijing 100084, China
email: dong_zhangyx@126.com

Wei-Xi Huang
Department of Engineering Mechanics
Tsinghua University
Beijing 100084, China
email: hwx@tsinghua.edu.cn

ABSTRACT

Numerical simulation is an important method to investigate the hydrodynamics of aquatic animals. However, the high Reynolds number (*Re*) simulation is a major challenge for such moving boundary problems and most work is limited the *Re* below 10^4. In the present study, we investigated the hydrodynamics and flow field of a forward swimming cow-nosed ray (Rhinoptera javanica) at $Re = 1.48 \times 10^5$. The computational model was constructed based on the biological data. A hybrid immersed boundary/wall-model approach for large eddy simulation was employed to simulate the high-Reynolds number turbulent flow around the cow-nosed ray. The hydrodynamic characteristics and vortex evolution of the swimmer were investigated. The effects of *Re* were also analyzed.

INTRODUCTION

Among aquatic animals, batoid fish are known for their outstanding swimming abilities, such as high-speed swimming, high-efficiency cruising, and maneuverability. Batoid fish are special aquatic animals that have a dorsoventrally flattened body and expanded pectoral fins. They adopted pectoral-fin-based locomotion as their sole propulsion strategy. The hydrodynamic mechanisms behind their high-speed and high-efficiency propulsion are of particular interest to the design of high-performance underwater vehicles.

Batoid fish is known to have various locomotion modes from undulatory to oscillatory (Rosenberger, 2001). One parameter to distinguish the two modes is the wavenumber travelling on the fins. Undulatory motion is defined to have more than one wave present on the fins at a time, whereas oscillatory motion are thought to have less than half a wave. The typical species of the former include skates and most stingrays. Manta, cownose, eagle and bat rays employ the latter mode.

Dewey *et al.* (2012) studied the hydrodynamics of the batoid-inspired oscillating propulsion using a mechanical flexible fin at $Re = 11600$. DPIV was used to display the wake and the interconnected vortex rings was observed in a 2D form, i.e., leading edge vortices (LEVs) and trailing edge vortices (TEVs) become entangled with one another. Bottom Ii *et al.* (2016) simulated the swimming of stingrays at two different swimming speed. The fast-swimming stingray was found 12 % more efficient than the slow-swimming one. It was the first time to show the existence of LEV on stingrays and the LEV was related to the thrust and efficiency enhancement. Zhang *et al.* (2022*a*) performed a numerical study on the hydrodynamic enhancement mechanism in batoid fish swimming. LEV, TEV and tip vortex (TV) were observed to construct the main vortex structures. By using derivative-moment transformation (DMT)- based force analysis, at low speed, TV contributes most to the thrust, whereas the LEV and TEV are unfavourable to the thrust generation. On the contrary, at a fast speed, the role of LEV changes to a favourable effect on the thrust. The effect of wavenumber was shown to influence the effective angle of attack of the fins. A smaller wavenumber leads to a larger effective angle of attack, and thus the strongest vortices. However, wavenumber of 0.4 has an optimal balance between the thrust enhancement and weakness effect of different local structures. Also, works focusing on more topics of batoid fish can be found, such as the kinematics (Fish *et al.*, 2016), flexibility (Menzer *et al.*, 2022), the role of cephalic fins (Zhao *et al.*, 2021) of manta rays and hydrodynamic benefits of protruding eyes and mouth on stingrays (Mao *et al.*, 2021).

Numerical simulation is an important method in investigating the hydrodynamics of aquatic animals. However, the high Reynolds number (Re) associated with the complex body morphology and swimming kinematics are the major challenges for numerical simulation because it requires very fine grids to resolve the boundary layer and the flow. Most of the above studies used low Reynolds numbers to present the realistic swimming flow. However, batoid fish swims at higher Reynolds numbers. For example, cow-nosed rays swim at $Re = 5 \times 10^4$ - 3×10^5 (Zhang *et al.*, 2022*a*). Manta rays swim at $Re = 6.85 \times 10^5 - 7.71 \times 10^6$ (Fish *et al.*, 2016). These motions have located in the turbulent regime for the flow over a flat plate. Moreover, we have concluded the Reynolds number of recent works about more species and models in figure 1 (Zhang *et al.*, 2022*b*) and found that the high-*Re* investigation is rare, especially the numerical work. Zhang *et al.* (2018*a*,*b*) conducted some high-*Re* simulations, but 2D models were em-

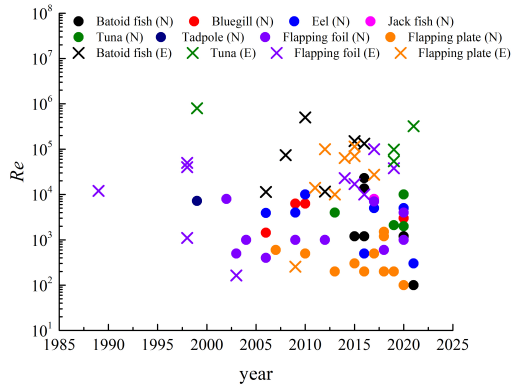

Figure 1. The Reynolds numbers used in recent works of swimming and flying; the circle represents high-fidelity numerical work (labelled by N) and the fork represents experimental work (labelled by E). Adapted with permission from Zhang *et al.* (2022*b*).

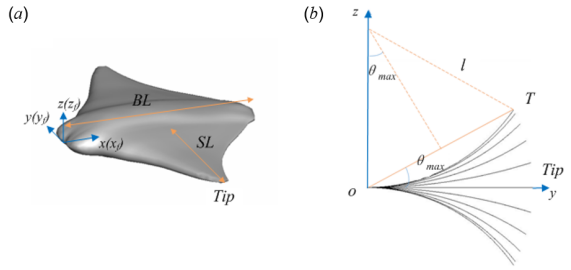

Figure 2. (*a*) The cow-nosed ray model in a flat position and the coordinate system for the kinematic model; (*b*) The spanwise deformation of the pectoral fin in the front view at different snapshots.

ployed in their work. To our knowledge, most numerical work of aquatic animals were limited the Re below 10^4. It is difficult to obtain the flow field information, which is significantly important in understanding the flow mechanisms of aquatic swimming, at such high Re. In the present work, we conducted a simulation of the flow of a cow-nosed ray swimming at $Re = 1.48 \times 10^5$.

COMPUTATIONAL MODEL

A three-dimensional (3D) model of the cow-nosed ray was constructed based on several section profiles, which can be seen from the previous study (Huang *et al.*, 2020). By the recordings of free-swimming cow-nosed ray specimens at an aquarium using a high-resolution digital camera, fin kinematic data were analysed. Some key points, such as the swimmers' head, tail base and pectoral fin tip were recorded. It was observed that the main deformation utilized by cow-nosed rays can be decomposed into spanwise deformation and chordwise deformation. We used a rotation around the longitudinal axis (x-axis) of the body and a chord-wise travelling wave to mathematical describe the above deformations, respectively. The mathematical approximation is introduced as follows (Zhang *et al.*, 2022*a*),

$$\begin{aligned} x(x_f,y_f,t) &= x_f \\ y(x_f,y_f,t) &= y_f(1-(1-k)|f(x_f,t)|y_f/SL)cos\theta(x_f,y_f,t) \\ z(x_f,y_f,t) &= z_f+y_f(1-(1-k)|f(x_f,t)|y_f/SL)sin\theta(x_f,y_f,t) \end{aligned} \tag{1}$$

$$\begin{aligned} \theta(x_f,y_f,t) &= \theta_{max}y_f/SL\cdot f(x_f,t) \\ f(x_f,t) &= sin(\omega t-2\pi W x_f/BL) \end{aligned} \tag{2}$$

where (x_f, y_f) defines the neutral plane of the pectoral fins in a flat position (figure 2*a*). At time t, the shape is described by the deformed coordinates (x, y, z). $W = BL/\lambda$ is the non-dimensional wavenumber, which is used to present the chordwise deformation. λ is the wavelength of the chordwise travelling wave. ω is the angular frequency. In order to fit the spanwise deformation, k and θ_{max} are used to control the parameters, whose meanings can be explained by figure 2*b*. It is assumed that the spanwise curve can be treated as an arc $\widehat{oT}$ with a radius of l. θ is the deviation angle, defined by the straight line oT joining the fin root and tip. The parameter k means the ratio of oT to its arc length $\widehat{oT}$, i.e., $k = 2lsin\theta_{max}/(l\cdot 2\theta_{max})$, when the fin tip reaches the highest position. θ_{max} is obtained by substituting $y_f = SL$ into the expression of $z(x_f,y_f,t)$ in equation (1), by providing the amplitude A. In our simulations, for the amplitude of A =0.6BL, a value of $\theta_{max} = 0.41$ and k = 0.972 can be determined for the model.

In order to simulate the high-Reynolds number turbulent flow over the complex moving boundaries, a hybrid immersed boundary (IB)/wall-model approach for large eddy simulation is employed. Details about this approach can be found in our previous work of Ma *et al.* (2019), so only brief descriptions are introduced here. The flow solver is governed the by filtered incompressible Navier-Stokes equations with an additional momentum force f_i.

$$\begin{aligned} \frac{\partial \tilde{u}_i}{\partial t}+\frac{\partial \tilde{u}_i\tilde{u}_j}{\partial x_j} &= \frac{\partial \tilde{p}}{\partial x_i}-\frac{\partial \tilde{\tau}_{ij}}{\partial x_j}+\frac{1}{Re}\frac{\partial \tilde{u}_i}{\partial x_j\partial x_j}+f_i \\ \frac{\partial \tilde{u}_i}{\partial x_i} &= 0 \end{aligned} \tag{3}$$

where $\tilde{u}_i$ is the filtered velocity components, $\tilde{p}$ is the filtered pressure. The large-scale structures of the turbulent flow field are directly resolved by the grid as the SGS structures and modelled using the Smagorinsky model. The additional force in the governing equations is calculated by a penalty method (Huang *et al.*, 2011) on the Lagrangian IB points.

To implement the wall model, the thin boundary layer equation was solved on an embedded mesh refined along the wall-normal direction and a dynamic matching procedure was adopted. This solver has been successfully applied in simulations of flapping propulsion, and validations can be also found in the previous studies (Ma *et al.*, 2019, 2021).

RESULTS

We conducted the simulations at the Reynolds number for a realistic cow-nosed ray , $Re = 1.48 \times 10^5$. In order to detect some differences at such a high Reynolds number, another simulations were also performed at $Re = 1.48 \times 10^4$ for comparison. The frequency f and tip-to-tip amplitude A are set at

0.7 Hz and $0.6BL$, respectively, resulting in a Strouhal number of 0.39. It is well known that many swimming animals are observed to cruise in a narrow range of Strouhal numbers ($0.2 \sim 0.4$) (Triantafyllou *et al.*, 1991). Such parameters are also in the range of those observed in most batoid fishes (Rosenberger, 2001; Zhang *et al.*, 2022*a*).

Hydrodynamic force

Figure 3a presents the instantaneous thrust which was normalized by $0.5\rho u^2 BL^2$. Around the mid-upstroke ($t/T = 0.3$) or mid-downstroke ($t/T = 0.8$), it produces a thrust peak, whereas it produces a drag peak as the fin reverses its stroke. By decomposing the total force into pressure (figure 3b) and viscous components (figure 3c), we found the main source of the thrust comes from the pressure force. Compared with the hydrodynamic performance at a lower Re (1.48×10^4), the thrust improves significantly with the increase of Re. The thrust enhancement comes from both the pressure and viscous force. From figure 3b the pressure force peak is enhanced by 83 %, and the viscous force decreases by 60 %. Those are due to that the high Re condition changes the flow around the swimmer, which is analysed in the following section. Notably, although the force value varies along with Re, the temporal variation tendency changes little. This coincides with previous study (Bozkurttas *et al.*, 2009) as the Reynolds number increases from 540 to 6300, for a bluegill sunfish. Our result indicates that this tendency remains the same for the flow at the Reynolds number of the order of 10^5.

Vortex dynamics

Figure 4 displays the vortex evolution of the swimming cow-nosed ray at $Re = 1.48 \times 10^5$, visualized by the isosurface of $Q = 500$ and colored by streamwise velocity. Figures 4a - 4c denote the downstroke, whereas figures 4d - 4f denote the upstroke. At $t/T = 0.17$, the boundary layer separates at the leading edge and formed a leading-edge vortex (LEV). The LEV structure breaks up into several co-rotating vortical structures. Similar phenomenon was also detected in revolving insect wings (Chen *et al.*, 2017). However, there form more vortices in the present work. At $t/T = 0.33$, as the LEVs convect downstream, the vortex cores are less diffused, especially at the tip region. At $t/T = 0.5$, there are no obvious coherent LEV structures, associating with the shed of tip vortices (TVs). Small-scale turbulent structures are likely to be dominant at the posterior of the cow-nosed ray and it forms hairpin vortices in the wake. At the dorsal of the cow-nosed ray, it also generates the hairpin vortices as seen in the enlarged view of figure 5. Two hairpin vortices packets, one containing five hairpins, another containing two hairpins, can be clearly observed. Such structures are usually detected in wall turbulence (Adrian, 2007). The existence of the hairpin on aquatic animals indicates that the flow is turbulent at the realistic Reynolds numbers. During the upstroke ($t/T = 0.67 - 1$), the broken LEVs keep convecting to the wake. Meanwhile, the repeated process takes place at the lower side of the pectoral fins.

For comparison, figure 6 gives the vortex structures at $Re = 1.48 \times 10^4$. The LEVs are also observed to break into several structures. However, larger-scale coherent structures dominate the flow, even in the wake when the structures are shed from the surface. Notably, at the dorsal of the cow-nosed ray, no hairpin vortices are formed.

Figure 7 displays the pressure distribution at the two Reynolds numbers during the downstroke. The attachment of

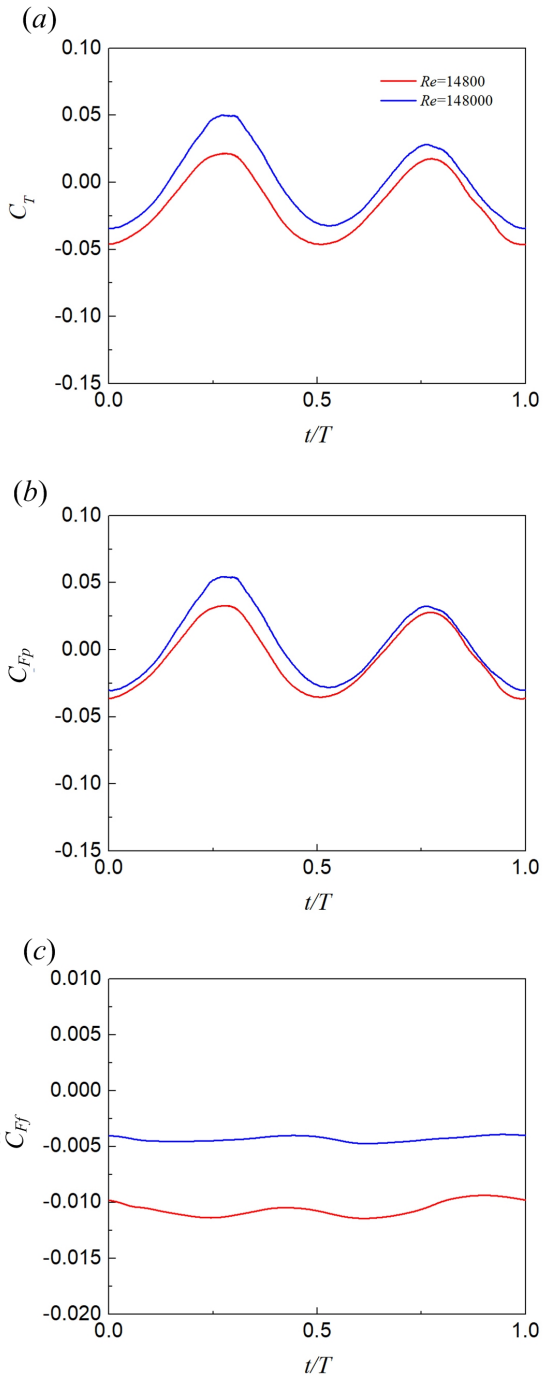

Figure 3. Time histories of the (a) total thrust force, (b) pressure force component and (c) friction force component of a swimming cow-nosed ray at $Re = 1.48 \times 10^4$ and 1.48×10^5.

LEV produces a low-pressure region near the leading edge. We can observe the moving of such low-pressure region with the convection of LEVs. The multiple LEVs create a long narrow band, which can be seen in figures 7a and 7d. At the dorsal of the surface, the existence of hairpin vortex produces some short low-pressure bands at $Re = 1.48 \times 10^5$, whereas such band does not occur at $Re = 1.48 \times 10^4$. Another difference is that it produces a stronger pressure fluctuation, which gives the evidence that the flow at such Re is turbulent. To describe the pressure difference due to the Reynolds number, the spanwise vorticity contours and pressure distribution along the chord at the plane of $z/SL = 0.31, 0.62$ are shown in figure 8. As shown

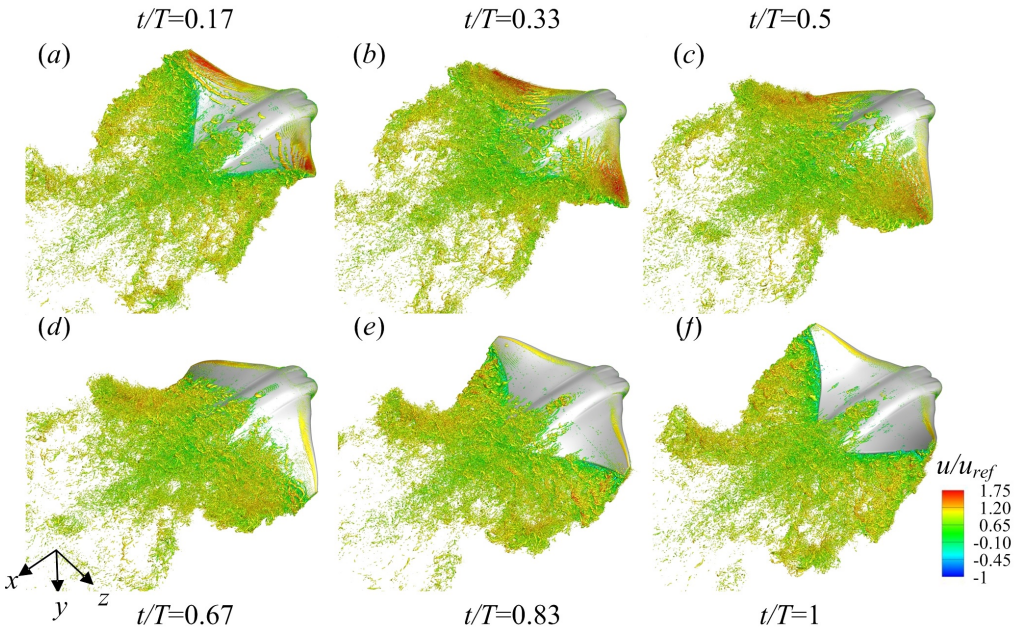

Figure 4. The instantaneous vortical structures of the swimming cow-nosed ray at $Re = 1.48 \times 10^5$, visualized by the isosurface of $Q = 500$ and colored by streamwise velocity. u_ref is the reference velocity at incoming flow.

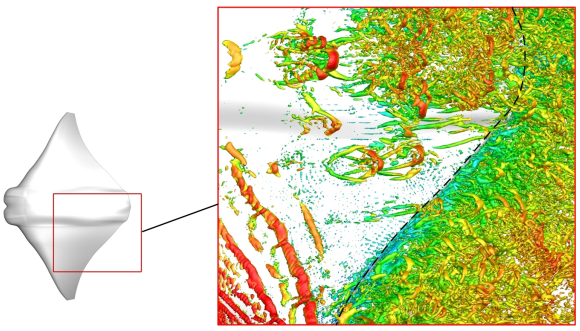

Figure 5. The enlarged view of vortical structures to show the multiple LEVs and hairpin vortices at $Re = 1.48 \times 10^5$.

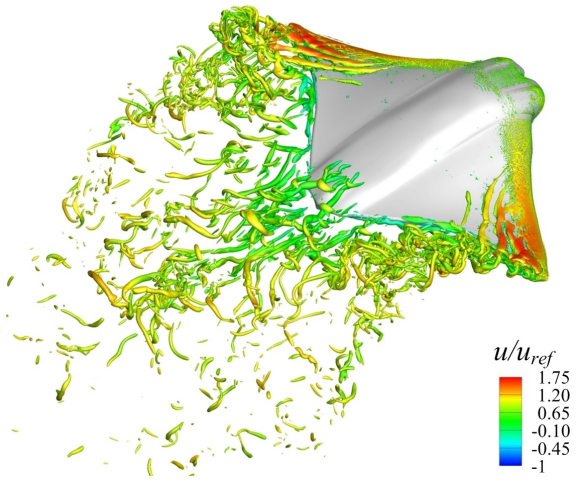

Figure 6. The vortical structures of the swimming cow-nosed ray at $Re = 1.48 \times 10^4$, visualized by the isosurface of $Q = 300$ and colored by the streamwise velocity.

in figure 8a, the attachment of LEV is truly observed to generate a pressure valley, corresponding the low-pressure region in figure 7 and the valley value is smaller for the high-*Re* flow. From the figure 8b, we can see that the pressure difference between the leading edge and trailing edge is larger for the high-*Re* case, creating a higher thrust force. Moreover, the stronger fluctuation shown in figure 8b provides visible evidence of the transition from laminar to turbulence.

From the shear distribution (figure 9) of the surface, it apparently shows that the high shear region locates at the leading edge of the model at $Re = 1.48 \times 10^5$. At $Re = 1.48 \times 10^4$, almost half of the whole body are occupied by the high shear region and the shear peak is higher than that at high Reynolds number, which gives an explanation to its high viscous force.

CONCLUSIONS

In the present study, we investigated the hydrodynamics and flow field of a forward swimming cow-nosed ray (Rhinoptera javanica) at Re, as high as 1.48×10^5, which is in the *Re* range of real swimming. We constructed a computational model based on biological data. A hybrid immersed boundary/wall-model approach for large eddy simulation was employed to simulate the high-Reynolds number turbulent flow. We traced the evolution of the LEV and found the hairpin vortices at the dorsal and wake of cow-nosed rays. The LEV to hairpin vortices transformation suggested a laminar to turbulent flow transition, whereas it does not take place at 1.48×10^4. Such transition leads to a change in the pressure and shear force distributions. As a result, the pressure component of the thrust force improves and the viscous component decreases; thus, The thrust force is enhanced as the Reynolds number increases. As stated in the introduction, the Reynolds number is limited to 10^4 for most previous studies. The present work gave an evidence that the force at low-*Re* condition can reflect the real hydrodynamics, at least below 10^5. However, when the attention is focused at the characteristics related to fluctuations, such as acoustics, high *Re* simulation is needed. Our work gives an insight into the understanding of the real-

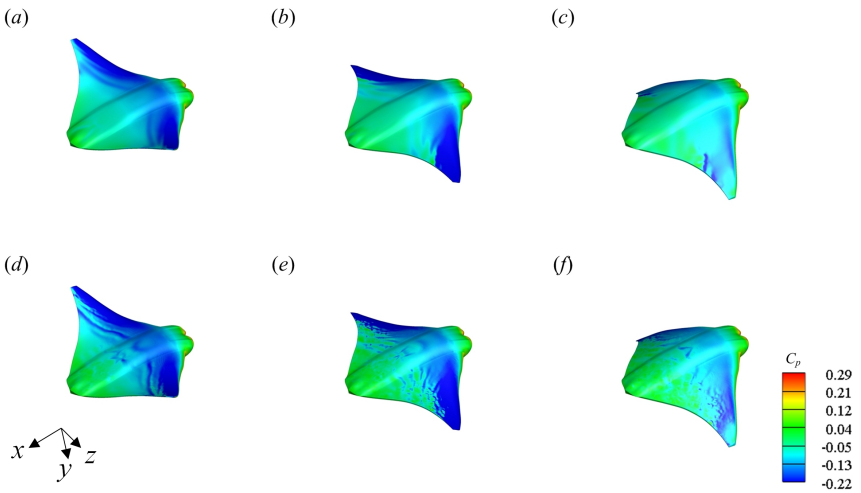

Figure 7. The surface pressure distributions at (a),(d) $t/T = 0.17$, (b),(e) $t/T = 0.33$, (c),(f) $t/T = 0.5$, at $(a-c)$ $Re = 1.48 \times 10^4$ and $(d-f)$ $Re = 1.48 \times 10^5$.

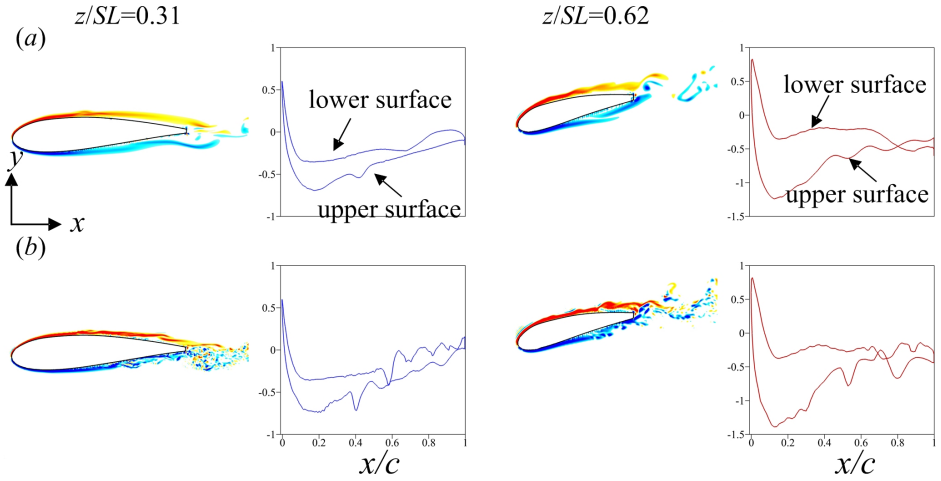

Figure 8. The spanwise vorticity contours and pressure distribution along the chord at the plane of $z/SL = 0.31, 0.62$, at (a) $Re = 1.48 \times 10^4$ and (b) $Re = 1.48 \times 10^5$.

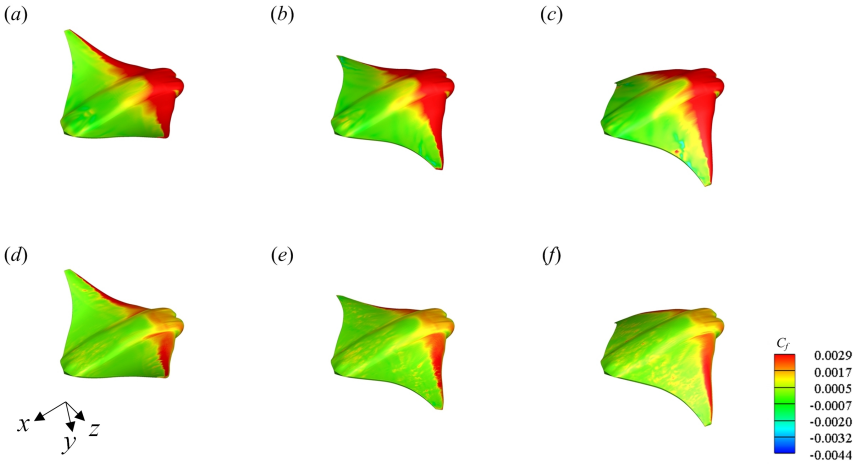

Figure 9. The surface shear distributions at (a),(d) $t/T = 0.17$, (b),(e) $t/T = 0.33$, (c),(f) $t/T = 0.5$, at $(a-c)$ $Re = 1.48 \times 10^4$ and $(d-f)$ $Re = 1.48 \times 10^5$.

istic turbulent flow of aquatic swimming and may inspire the design of biomimetic propulsors in the real environment.

ACKNOWLEDGEMENTS

The authors acknowledge funding support from the National Natural Science Foundation of China (Grant Numbers 12102227 and 11772172) and China Postdoctoral Science Foundation (Grant Number 2022M711754).

REFERENCES

Adrian, Ronald J 2007 Hairpin vortex organization in wall turbulence. *Physics of fluids* **19** (4), 041301.

Bottom Ii, RG, Borazjani, I, Blevins, EL & Lauder, GV 2016 Hydrodynamics of swimming in stingrays: numerical simulations and the role of the leading-edge vortex. *Journal of Fluid Mechanics* **788**, 407–443.

Bozkurttas, M, Mittal, R, Dong, H, Lauder, GV & Madden, P 2009 Low-dimensional models and performance scaling of a highly deformable fish pectoral fin. *Journal of Fluid Mechanics* **631**, 311–342.

Chen, Di, Kolomenskiy, Dmitry, Nakata, Toshiyuki & Liu, Hao 2017 Forewings match the formation of leading-edge vortices and dominate aerodynamic force production in revolving insect wings. *Bioinspiration & biomimetics* **13** (1), 016009.

Dewey, Peter A, Carriou, Antoine & Smits, Alexander J 2012 On the relationship between efficiency and wake structure of a batoid-inspired oscillating fin. *Journal of fluid mechanics* **691**, 245–266.

Fish, F. E., Schreiber, C. M., Moored, K. W., Liu, G., Dong, H. & Bart-Smith, H. 2016 Hydrodynamic performance of aquatic flapping: efficiency of underwater flight in the manta. *Aerospace* **3** (3), 20.

Huang, Q., Zhang, D. & Pan, G. 2020 Computational model construction and analysis of the hydrodynamics of a rhinoptera javanica. *IEEE Access* **8**, 30410–30420.

Huang, W. X., Chang, C. B. & Sung, H. J. 2011 An improved penalty immersed boundary method for fluid–flexible body interaction. *Journal of Computational Physics* **230** (12), 5061–5079.

Ma, M., Huang, W. X. & Xu, C. X. 2019 A dynamic wall model for large eddy simulation of turbulent flow over complex/moving boundaries based on the immersed boundary method. *Physics of Fluids* **31** (11), 115101.

Ma, M., Huang, W. X., Xu, C. X. & Cui, G. X. 2021 A hybrid immersed boundary/wall-model approach for large-eddy simulation of high-reynolds-number turbulent flows. *International Journal of Heat and Fluid Flow* **88**, 108769.

Mao, Qian, Zhao, Jiazhen, Liu, Yingzheng & Sung, Hyung Jin 2021 Hydrodynamic benefits of protruding eyes and mouth in a self-propelled flexible stingray. *Physics of Fluids* **33** (8), 081915.

Menzer, Alec, Gong, Yuchen, Fish, Frank E & Dong, Haibo 2022 Bio-inspired propulsion: Towards understanding the role of pectoral fin kinematics in manta-like swimming. *Biomimetics* **7** (2), 45.

Rosenberger, Lisa J 2001 Pectoral fin locomotion in batoid fishes: undulation versus oscillation. *Journal of Experimental Biology* **204** (2), 379–394.

Triantafyllou, MS, Triantafyllou, GS & Gopalkrishnan, R 1991 Wake mechanics for thrust generation in oscillating foils. *Physics of Fluids A: Fluid Dynamics* **3** (12), 2835–2837.

Zhang, D., Huang, Q., Pan, G., Yang, L. & Huang, W. X. 2022*a* Vortex dynamics and hydrodynamic performance enhancement mechanism in batoid fish oscillatory swimming. *Journal of Fluid Mechanics* **930**, A28.

Zhang, Dong, Pan, Guang, Chao, Liming & Yan, Guoxin 2018*a* Mechanisms influencing the efficiency of aquatic locomotion. *Modern Physics Letters B* **32** (25), 1850299.

Zhang, Dong, Pan, Guang, Chao, Liming & Zhang, Ya 2018*b* Effects of reynolds number and thickness on an undulatory self-propelled foil. *Physics of Fluids* **30** (7), 071902.

Zhang, Dong, Zhang, Jun-Duo & Huang, Wei-Xi 2022*b* Physical models and vortex dynamics of swimming and flying: a review. *Acta Mechanica* pp. 1–40.

Zhao, Jiazhen, Mao, Qian, Pan, Guang, Huang, QiaoGao & Sung, Hyung Jin 2021 Hydrodynamic benefit of cephalic fins in a self-propelled flexible manta ray. *Physics of Fluids* **33** (8), 081906.